JOURNAL OF MATERIALS SCIENCE 13 (1978) 2587–2599

Structural relaxation in amorphous $Fe_{40}Ni_{40}P_{14}B_6$ studied by energy dispersive X-ray diffraction*

T. EGAMI
Department of Metallurgy and Materials Science and Laboratory for Research on the Structure of Matter, University of Pennsylvania, Philadelphia, Pa 19104, USA

The atomic structure and the structural relaxation of amorphous $Fe_{40}Ni_{40}P_{14}B_6$ alloy were studied using the energy dispersive X-ray diffraction method. It was demonstrated that the structure of the amorphous alloy can be determined self-consistently with high accuracy by this method. The results indicated that the structural relaxation is a highly collective process involving many atoms, and can be described in terms of the redistribution and transformation of the structural defects.

1. Introduction

Amorphous metallic alloys, also known as metallic glasses, can be prepared by various methods and for a fairly wide range of composition [1]. They were initially regarded as pure laboratory curiosities. However, as production methods were improved and their excellent magnetic, mechanical and chemical properties became known, they quickly gained recognition as possible engineering materials [2]. In the past five to six years, particularly after Allied Chemical Co. started production of these materials, the properties of amorphous alloys have been extensively studied by various methods. They include structural, mechanical, magnetic, electric, and thermal properties. Through these studies, it became clear that many of these properties are often drastically changed by annealing without causing crystallization. Some of these effects of annealing, such as a decrease in magnetic anisotropy [3] or stress relief [4, 5], are the results of ordinary diffusion, but many are attributed to a subtle change in the structure, usually called the structural relaxation. Amorphous alloys are usually obtained by rapid quenching; the liquid state can be preserved by quickly freezing the liquid, i.e., by cooling down below the glass transition temperature T_g, before the nucleation of the crystalline state [6–8]. During the rapid quenching, the atoms usually have insufficient time to relax from the high temperature atomic configuration to the low temperature configuration, therefore the frozen liquid stays in a metastable state, not only with respect to the crystalline state, but also with respect to a relaxed, more stable glassy state. The structural relaxation occurs when this metastable frozen liquid relaxes into a more stable state when annealed. Such a phenomenon is quite commonly observed in inorganic or organic (high polymer) glasses, and has been extensively studied [9–11]. A concept which is often used to explain the structural relaxation in polymer glass is the excess free volume [10]. The free volume [12] in the liquid or glassy state is the analogue of the vacancy in crystalline solids. The equilibrium amount of free volume in the liquid is a function of temperature, and is directly related to the viscosity. As the liquid is cooled down, the amount of free volume is decreased, so that the viscosity is increased. The glass transition temperature is defined as the temperature at which the viscosity has increased to some specific value (usually 10^{13} poise). The reduction in the free volume, however, does not occur instantaneously, since the free volume somehow has to reach the surface of the liquid. The rate of this process is determined by the diffusivity, or the viscosity itself. Therefore, if the cooling rate is sufficiently high, the glass

* Supported by NSF through Grant DMR 75-15633 and MRL Grant DMR 76-80994

transition is reached before all the free volume reaches the surface, and the excess free volume will be trapped inside the glass. The excess free volume is annealed out as the structural relaxation occurs. As will be shown in the present paper, the concept of free volume is less directly applicable to the amorphous metallic alloys than to high polymer glasses. However, if an appropriate defect is defined, the explanation above seems to be perfectly valid when the concept of free volume is replaced by such a defect.

The structural relaxation of amorphous metallic alloys has been indirectly observed by means of the internal friction and elastic constant [13–15], specific heat [16], stress relaxation [17] and mechanical creep [18]. A direct indication of structural change has been observed by X-ray diffraction by Waseda and Masumoto [19]. The change, however, was too small for conventional X-ray diffractometry to allow a reliable interpretation. A more recent study by Graczyk using electron diffraction revealed a sizeable structural change upon annealing [20]. However, this study was made on thin films of transition metal–rare earth amorphous alloys containing a fair amount of oxygen. Therefore, its generality as a study of structural relaxation in amorphous metallic alloys is somewhat questionable.

In the present paper, we report our study of the structural relaxation in amorphous $Fe_{40}Ni_{40}P_{14}B_6$ (Allied Chemical Metglas alloy 2826) obtained by a splat cooling technique [21]. This alloy was chosen despite its complex chemical composition, partly because it can be obtained in a better form than others, in terms of width, surface conditions, geometrical uniformity and stability, and also because the annealing behaviour of this alloy has been most extensively studied. In order to observe small changes in the structure, the technique of energy dispersive X-ray diffraction (abbreviated as EDXD hereafter) was used. The structural relaxation studied here is topological short-range ordering of the metal atoms. The X-ray detects mainly the position of the transition metal atoms, not the metalloid atoms, and does not distinguish between Fe and Ni. There is another structural relaxation process in which compositional short range ordering of transition metals (in this case Fe and Ni) seems to occur [22]. This process can be detected by magnetic measurements [23], but not by EDXD in its present form, since the X-ray scattering factors of Fe and Ni are too similar.

The EDXD method using a solid-state detector was first employed by Giessen and Gordon [24], and recently applied to a structural study of liquid Hg by Prober and Schultz [25]. Unlike the conventional angular-scanning diffraction using a monochromatic X-ray source, the EDXD method utilizes white X-ray radiation and a fixed diffraction angle. At fixed angle, the scattering vector is proportional to the energy of the incident photon. Therefore, the diffracted intensity spectrum (as a function of energy) contains the same structural information as can be obtained by a conventional diffraction measurement [26]. Recent progress in energy-sensitive photon detectors has enabled the determination of the intensity spectrum with satisfactory resolution and efficiency, and has made the EDXD method not only practical but also advantageous over the conventional diffraction method in terms of the statistical accuracy. This improved accuracy is achieved for several reasons: (a) since the counting of photons with different energies is done simultaneously, fluctuations in the intensity of the X-ray source does not affect the result; (b) no mechanically moving parts are required, and (c) the total intensity of the white X-ray radiation is usually higher than the intensity of the characteristic radiation. Furthermore, the use of higher energy photons (up to 48 keV) makes it possible to determine the structure factor to higher values of the wave vector q. The main disadvantages of the EDXD method are the limited resolution of the detector (in our case ~150 eV at 6 keV, and ~230 eV at 40 keV), and the need for a fairly complex and so far unestablished method of data processing. In this paper, we first demonstrate that an equation for the diffracted intensity spectrum can be derived which leads to a self-consistent determination of the structure factor, and then by annealing the sample in place in the diffractometer, we show that the structural relaxation can be studied with high accuracy, taking full advantage of the fact that no moving parts are involved in the EDXD system.

2. Experimental

A schematic of our EDXD system is shown in Fig. 1. The tungsten-target X-ray tube was operated at 48 kV, with a beam current of 14 or 20 mA (full-wave) with or without a constant potential unit. The use of the constant potential unit makes no difference to the long-term stability

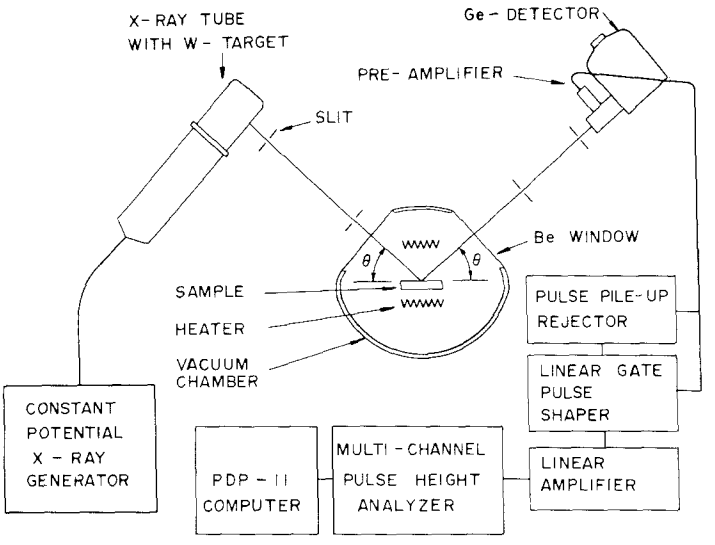

Figure 1 Schematic diagram of the EDXD system.

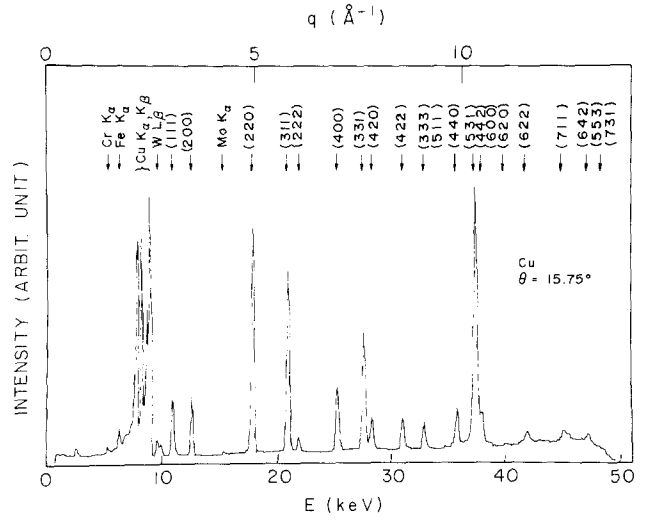

Figure 2 Diffraction pattern of polycrystalline copper stored in MCA; the x–y recorder trace. Weak characteristic radiations are either due to contamination in the X-ray target (Mo) or impurities in copper (Fe, Cr).

of the X-ray generation, but helps to increase the intensity of higher energy X-rays and to reduce the polarization of low energy X-rays. The optical system of the unit (slits) was made as simple as possible, in order to avoid fluorescence. The sizes of the slits are changed as the diffraction angle is changed, and also depending on the purpose of the diffraction, i.e., whether the aim is to measure the structure itself or to study the structure relaxation. For the study of structure, the resolution of the optical system was set to about 1%. Fig. 2 shows the diffraction pattern of crystalline Cu, indicating that the overall resolution (the optical resolution plus the resolution of the detector) is about 2%, which is good enough to study the non-crystalline solids. A slightly lower resolution (4%) was used for the study of structural relaxation for the purpose of increasing the photon count rate.

As a detector, an intrinsic Ge detector (Princeton Gamma-Tech) was used. A pulse pile-up rejector and a pulse shaper were added to improve the accuracy of counting at higher counting rates. With a pulse-shaping time of 6 μs, the resolution of the detector did not deteriorate appreciably up to a counting rate of 10^4 photon s^{-1}, but usually the counting rate was kept down to 10^3 photon s^{-1}, to insure the accuracy of the result. Even at this rate, the counting is significantly faster than in a conventional diffraction measurement. The channel width of the MCA was usually set to 100 eV, so that 500 channels cover the entire spectrum. The total photon count was 10^6 to 10^7 for the study of structure and $\sim 5 \times 10^7$ for the study of relaxation. The data were processed by a PDP-11/10 minicomputer.

The determination of the structure factor, or

the interference function $i(q)$, was made in the reflection geometry with the sample thick enough (0.9 mm) to make the absorption correction simpler. The sample as-received was in the form of a long ribbon 60 μm thick and 2 mm wide. Fifteen layers of ribbon, each layer consisting of 6 strips of 2 cm long ribbon laid side by side, were fixed on a stainless steel plate. The steel backing was chosen so that any X-ray photons penetrating the sample (maximum 3% at 40 keV) can be reflected in a similar manner to the sample. The top layer of the sample was mechanically polished to remove surface contamination.

The structural relaxation, on the other hand, was studied in the transmission geometry, because monitoring of the fluorescence yield from the sample indicated that surface reconstruction during annealing interfered with the measurement in low-angle reflection. The surfaces of the sample were carefully polished, first mechanically, and then electrochemically, in a bath of 10% perchloric acid and 90% alcohol at 0° C with an applied potential of 12 V. The sample thickness was reduced from 60 μm to 50 μm by polishing. Short sections of ribbon sample were spot-welded to a stainless steel frame in two layers, and then placed in a small vacuum chamber with beryllium windows and an internal heater, which was evacuated by a sorption pump. The chamber was water-cooled to protect the beryllium window seals and to insure a sufficient cooling rate for the sample. The usual heating and cooling rate of the sample for the annealing was 25 to 30° C min^{-1} and 15° C min^{-1}, respectively.

3. Determination of the radial distribution function (RDF)

It can be shown that the intensity of the diffracted X-ray in the reflection geometry (for an infinitely thick sample) is given by

$$I_s(E) = \frac{2}{\mu(E)+\mu(E')} P(E',\theta)\,\langle f_c(q')\rangle I_p(E') + \frac{1}{\mu(E)}\,[i(q)\,\langle f\rangle\langle f^*\rangle + \langle ff^*\rangle]\,P(E,\theta) I_p(E) \tag{1}$$

where $I_p(E)$ is the spectral intensity of the primary beam, $P(E, \theta)$ the polarization factor, $\mu(E)$ the absorption coefficient of the sample, $f_c(q)$ the Compton scattering intensity, $f(q)$ the atomic scattering factor, $\langle \ldots \rangle$ the compositional average, $i(q)$ the interference function, $q = E/\hbar c$, $q' = E'/\hbar c$ and E' is the initial photon energy which is reduced to E after the Compton scattering, or

$$E' = E + \Delta E = E/(1 - 0.00391\,E \sin^2\theta) \quad (E \text{ in keV}) \tag{2}$$

The Compton shift ΔE in fact has a width, but neglecting the profile seems to give good enough results. The neglect of the shift itself, however, leads to a serious error when $\langle f_c(q)\rangle$ is not small compared to $\langle ff^*\rangle$. Prober and Schulz [25] had success even neglecting ΔE, since f_c is much smaller than $|f|^2$ in Hg. Among the quantities in Equation 1, $\mu(E)$ and the energy independent part of the scattering factor can be obtained from standard sources [27], but the anomalous dispersions f' and f'' are available only for certain energies, so that they had to be calculated for general energy using the cross-sections computed by Cromer and Liebermann [28] and the equation of Parratt and Hempstead [29]. The Compton scattering intensity, $f_c(q)$, was obtained from the Compton scattering factor, $I_c(q)$, calculated by Cromer [30, 31]. As has been recognised earlier [25], the Breit–Dirac recoil factor, R, should be given by

$$R = (E/E')^2 \tag{3}$$

for the photon counter rather than $(E/E')^3$, and the calculated intensity $I_c(q)$ should be multiplied by this factor to yield the observed intensity. However, the Compton scatterings observed in the energy range from E to $E + dE$ come from the incident photons whose energies range from E' to $E' + dE'$. Since,

$$\frac{dE'}{dE} = \left(\frac{E'}{E}\right)^2 \tag{4}$$

this factor exactly cancels the Breit–Dirac factor, so that the Compton scattering intensity for the EDXD measurement should just be equal to $I_c(q)$, rather than $R \cdot I_c(q)$.

The greatest difficulty in using the EDXD method is that the intensity and the polarization of the incident X-ray cannot be easily known. These quantities can only be determined experimentally, since they are the variables of each X-ray generating system. We followed, with modifications, the suggestion by Prober and Schultz to use the very sample to be studied. They suggested that $i(q)$ is negligibly small for high

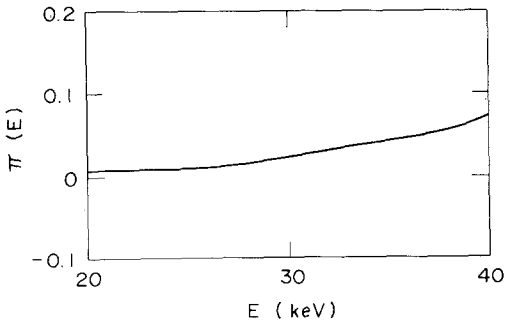

Figure 3 Energy dependence of the polarizability, $\pi(E)$, for the particular X-ray tube used in the present study.

values of q, so that the high angle run should give values of $\hat{I}_p(E) = I_p(E)/\mu(E)$ when divided by the theoretical intensity $\langle f^2 \rangle + \langle f_c \rangle$. This simple method, however, does not work very well in the present case in which the effect of the Compton shift is quite significant. The polarization factor

$$P(E, \theta) = [(1 + \cos^2 2\theta)/2] - [(1 - \cos^2 2\theta)/2]\, \pi(E) \quad (5)$$

(Fig. 3) and $\hat{I}_p(E)$ (Fig. 4) were then determined using the data from four runs. The details of our method are described in the Appendix. Since $\hat{I}_p(E)$ has a peak at around 30 keV, the energy region from 20 keV to 40 keV was used for analysis. In the energy region lower than 20 keV, we have problems with the Mo contamination in the W target of the X-ray tube, fluorescense from the sample and their two-photon peaks, and also high absorption. In the energy region higher than 40 keV, the primary intensity is low and the polarization correction becomes rather large.

Now that Equation 1 is completely given apart from the factor $i(q)$, it can be used for the structural determination. The crucial test of Equation 1 was then made with a run at $\theta = 42.4°$. Since $i(q)$ is very small in the range of q covered by this run, the diffracted intensity spectrum is rather featureless (Fig. 5). Then the observed spectrum I_{obs} should be almost proportional to the calculated intensity using Equation 1 but assuming $i(q) = 0$. Fig. 6 shows that this is true, within 1%, up to 36 keV and within 5% at 40 keV. The greater deviation at higher energy is probably because the scattering factor is reliable only up to 25 $Å^{-1}$. The neglect of the Compton shift itself in Equation 1 results in a drop of I_{obs}/I_{calc} by as much as 20% on going from 20 keV to 40 keV. In our view, the success of this test is critically important in demonstrating the accuracy of the structure determination by the EDXD method.

The values of $i(q)$ for amorphous $Fe_{40}Ni_{40}P_{14}B_6$ alloy were then determined, using Equation 1, from seven runs at different angles. The run at the lowest angle (4.32°) covering the q-space below 2.9 $Å^{-1}$ was done in transmission geometry, to avoid the spurious scattering from the oxide layer on the surface of the sample. Seven runs were used in order to have enough overlap in q-space from run to run so that the self-consistency of the results could be checked for all q. Starting with the run at the highest scattering angle ($\theta = 42.4°$), $i(q)$ was determined down to the lowest value in

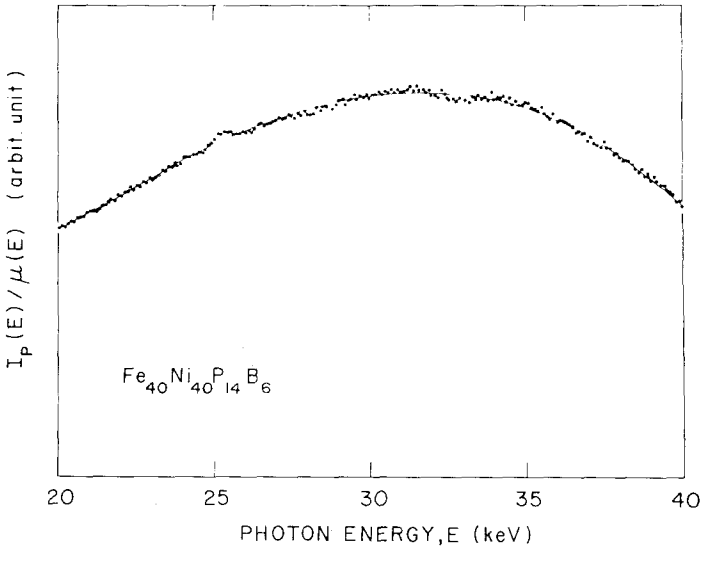

Figure 4 Spectrum of the X-ray source intensity, $I_p(E)/\mu(E)$. The solid line is the least square fit by a polynomial.

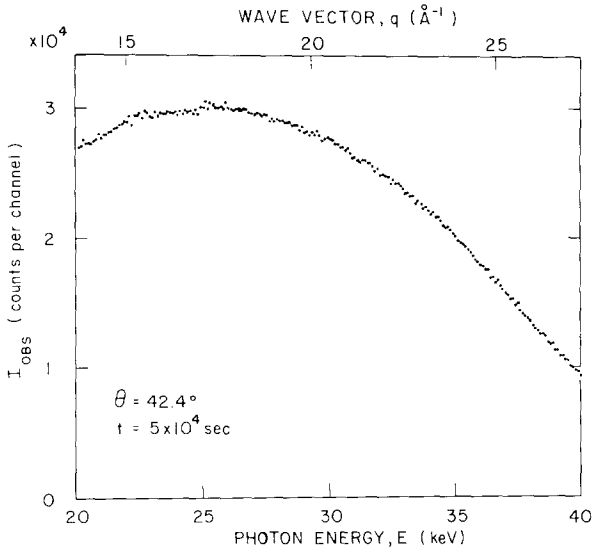

Figure 5 Diffraction spectrum at $\theta = 42.4°$.

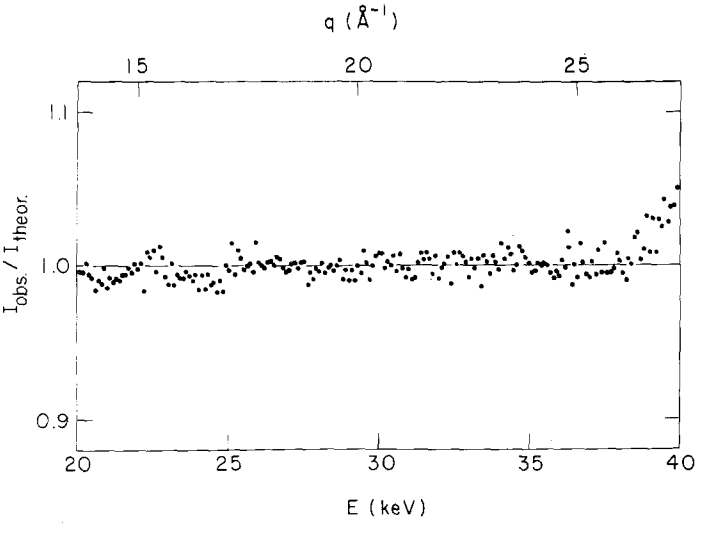

Figure 6 Diffraction spectrum at $\theta = 42.4°$, divided by Equation 1 assuming $i(q) = 0$. Deviations from unity at above $q = 26$ Å^{-1} are because the scattering factor is given reliably only up to 25 Å^{-1}.

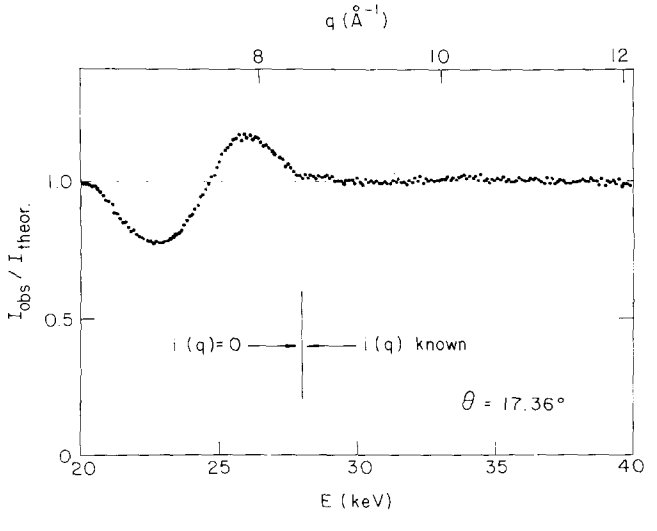

Figure 7 Diffraction spectrum at $\theta = 17.36°$, divided by Equation 1, with $i(q)$ determined for $q > 8.4$ Å^{-1}, but assumed to be zero for $q < 8.4$ Å^{-1}. That I_{obs}/I_{theor} is almost unity for $q > 8.4$ Å^{-1} indicates that the data obtained in this run are consistent with those at higher diffraction angles.

q which corresponds to the energy of 20 keV. We then considered the data at the next highest angle, checked the consistency in the overlapped q-space, and then determined $i(q)$ to the lower values in q down to the limiting value of q in this run. An example is shown in Fig. 7. In this case, $i(q)$ had been determined by previous runs down to $q_0 = 8.4\,\text{Å}^{-1}$, so that I_{obs}/I_{calc} [$i(q)$ is still assumed to be zero below q_0] is almost equal to unity above q_0, indicating sufficient consistency. The consistency was less satisfactory for the first peak in $i(q)$. This peak is fairly sharp, so that the difference in resolution between two runs yielded different peak heights (by about 3%); the low angle run with better resolution was chosen to determine $i(q)$. The values of $q \cdot i(q)$ thus determined are shown in Fig. 8, together with the difference in $q \cdot i(q)$ caused by annealing at 350° C for 30 min which will be discussed later in detail.

The effect of air scattering and multiple-scattering [32] was estimated to be of the order of 1 to 2%, but only weakly dependent on q. Since the accuracy in $i(q)$ thus determined was of the same magnitude, these effects were neglected in the present study. The radial distribution function (RDF) $\bar{\rho}(r)$ was then obtained by the Fourier transformation,

$$\bar{\rho}(r) - \rho_0 = \frac{1}{2\pi^2 r}\int i(q) \cdot \sin qr \cdot q \, dq. \quad (6)$$

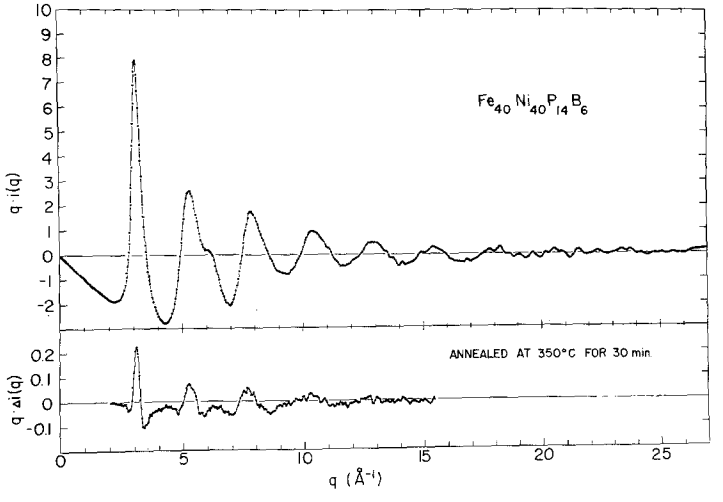

Figure 8 The interference function $q \cdot i(q)$ of $Fe_{40}Ni_{40}P_{14}B_6$ amorphous alloy, and the change in the interference function caused by the annealing treatment at 350° C for 30 min. Note that the scale of the difference $q \cdot \Delta i(q)$ is smaller by the factor of 10 than that of the interference function.

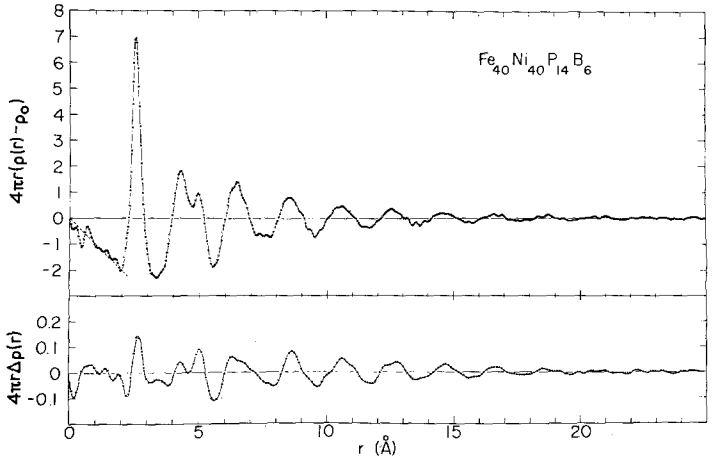

Figure 9 Radial distribution function of $Fe_{40}Ni_{40}P_{14}B_6$ amorphous alloy determined by the EDXD method, and the change in RDF caused by the annealing treatment at 350° C for 30 min.

Since the variation in $i(q)$ beyond 20 Å^{-1} appears to be mostly noise, $i(q)$ was multiplied by a damping factor of exp $[-0.03(q-18)^2]$ $(q>18$, value of q in Å^{-1}). This damping removed fast oscillations in RDF, but did not change the significant features such as the peak height. The result is presented in Fig. 9. As is well known, Equation 6 does not give the compositionally averaged RDF,

$$\langle \rho(r) \rangle = \sum_{ij} C_i C_j \rho_{ij}(r) \tag{7}$$

where C_i is the concentration of the ith element in the alloy specimen and $\rho_{ij}(r)$ is the partial RDF between the ith and jth elements, but rather

$$\bar{\rho}(r) = \sum_{ij} C_i C_j \int_0^\infty R_{ij}(r, r') \rho_{ij}(r') r'^2 \, dr' \tag{8}$$

where

$$R_{ij}(r, r') = \int_0^\infty \frac{f_i(q) \cdot f_j^*(q)}{\langle f \rangle \langle f^* \rangle} \frac{\sin qr}{qr} \frac{\sin qr'}{qr'} q^2 \, dq \tag{9}$$

and $f_i(q)$ is the scattering factor of the ith element. $R_{ij}(r, r')$ has a sharp peak at $r = r'$, so that $\bar{\rho}(r)$ is close to $\langle \rho(r) \rangle$.

However, in the present case, since f_{Fe} and f_{Ni} are similar, R_{Fe-Fe} and R_{Ni-Ni} have considerable ripples for small r. The noise for $r < 2$ Å seen in Fig. 9 is considered to be primarily due to this effect. The RDF thus obtained is in good agreement with that of the dense-random-packing-hard-sphere (DRPHS) model of Ichikawa for the tetrahedra parameter $k = 1.3$, including the small peak at 7.3 Å which corresponds to clusters of four collinear atoms [33]. The positions of the first and second peaks are in agreement with earlier works on similar alloy systems [34, 35]. Principal results are given in Table I.

4. Structural relaxation

As described earlier, the study of the change in $i(q)$ by annealing was made in transmission geometry, with the annealing done *in situ* in the diffractometer. Since the changes in the surface condition, such as oxidation, could easily introduce spurious changes in $i(q)$, the fluorescence yield from the sample was always monitored. If the fluorescence yield showed appreciable change (more than 1%), the result was rejected. The fluorescence line was also used to correct for the drift in the zero level of the MCA. The zero level was found to be rather sensitive to the ambient temperature, and was shifted by about 1/20 of the channel width for each degree change in temperature. Such a drift can sometimes be serious, since we are concerned with rather small changes in $i(q)$. The change in $i(q)$ was determined from runs at three angle settings, 7.23°, 13.25°, and 20.57°. The exposure times were 4×10^4 s, 5×10^4 s, and 3×10^5 s for these three angle settings, respectively. The medium angle (13.25°) run was repeated three times for different samples, and the average over the three runs was used. The results of high and low angle runs were smoothly joined to the values of $\Delta i(q)$ obtained from the medium angle runs. The noise at high q was damped by multiplying by exp $[-0.03(q-6)^2]$ for $q > 6$. The change in $i(q)$ due to annealing at 350° C for 30 min,

$$q \cdot \Delta i(q) = q [i_{\text{annealed}}(q) - i_{\text{as-received}}(q)] \tag{10}$$

is presented in Fig. 8, after multiplication by the damping factor. The statistical accuracy of the result is ±0.01. However, the overall accuracy is estimated to be about 20%, partly due to the resolution of the optical system which was somewhat sacrificed in order to increase the photon count.

TABLE I

	$Fe_{40}Ni_{40}P_{14}B_6$	$Ni_{80}P_{20}$ [35]	$Fe_{80}P_{13}C_7$ [19]
Position of the first peak in $i(q)$ (Å^{-1})	3.15	3.10	3.03
Position of the second peak in $i(q)$ (Å^{-1})	5.31	5.35	5.22
Position of the first peak in $\rho(r)$ (Å)	2.54	2.55	2.58
Position of the second peak in $\rho(r)$ (Å)	4.28	4.23	4.28
Position of the subpeak of the second peak in $\rho(r)$ (Å)	4.96	4.76	4.96
Co-ordination number	12.0	13.5	11.7

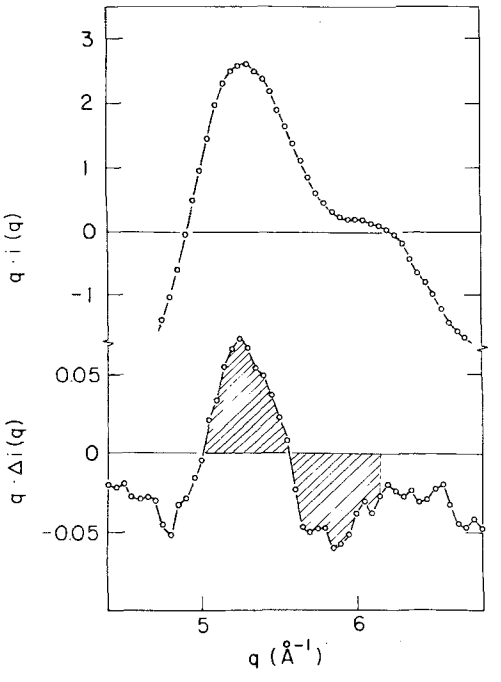

Figure 10 Second peak in $q \cdot i(q)$ (above) and the change $q \cdot \Delta i(q)$ due to annealing at 350° C for 30 min (below). The shaded area defines the relaxation parameter, Equation 11.

The Fourier transform of $q \cdot \Delta i(q)$ directly yields the change in the RDF, $4\pi r \Delta\rho(r)$ (Fig. 10). Note that the absolute accuracy of this quantity is higher than that of $\rho(r)$ itself, and is estimated to be about ± 0.03.

The result presented in Fig. 9 is quite informative about the nature of the structural relaxation. Firstly, the position of the nearest neighbour peak and its integrated density (co-ordination number) are basically *unchanged* by annealing. The nearest neighbour distance, in fact, is slightly increased (by about 10^{-3} Å) whereas the specific volume of the sample is decreased by a maximum of 0.5% [23]. This is presumably the direct reflection of the stronger repulsion (than attraction) of the inter-atomic potential. Secondly, in general the peaks become higher and the valleys become deeper. The split in the second peak particularly is enhanced by annealing. Thirdly, the relative changes in the first and second peaks are 2 to 3%, but the subpeak in the second peak and the third, fourth and fifth show changes as much as 5 to 10%.

These observations lead to the following important conclusions:

(a) The structural relaxation involves rather extensive changes in the atomic short-range order.

(b) The change in the nearest neighbour shell is not a change in the nearest neighbour distance, but a rearrangement among the neighbouring atoms without changing the distance.

(c) The basic structural units, such as tetrahedra, are hardly affected by relaxation except for slight distortions. However, the relative configurations of such units are changed during the relaxation. Therefore, the structural relaxation is a highly collective phenomena, involving the motion of a number of atoms.

5. Kinetics of structural relaxation

As has been described elsewhere [36], it is possible to study the kinetics of the structural relaxation directly from the change in $i(q)$. Although $\Delta\rho(r)$ was calculated only for a specific annealing condition, it appears that the salient features of the structural change, such as the narrowing of the first peak, the increase in the second peak height and the decrease in the height of the shoulder of the second peak, are commonly found for any annealing temperature and time. Therefore, the kinetics of the relaxation can be described by the kinetics of one of these features, without obtaining the entire $\Delta i(q)$ for each annealing treatment. We singled out as a convenient parameter the change in the second peak, defined by the shaded area in Fig. 10:

$$R(T_a, t_a) = \frac{1}{q_2 - q_1} \int_{q_1}^{q_2} |\Delta i(q)| \cdot q \cdot dq \qquad (q_1 = 5\,\text{Å}^{-1}, q_2 = 6.15\,\text{Å}^{-1}) \tag{11}$$

where T_a is the annealing temperature and t_a is the annealing time. $R(T_a, t_a)$, thus defined, is not only convenient for measurement but clearly separates the relaxation process from the crystallization process, since, as shown in Fig. 11, the change in $i(q)$ when the sample starts to crystallize is totally opposite: the second peak becomes lower and the shoulder becomes higher and grows into a diffraction peak. This is not the case for other peaks; both the first and the third peaks become higher because of structural relaxation, and increase even more when crystallization occurs.

The time and temperature dependence of the relaxation parameter is shown in Fig. 12. It was found that

$$R(T_a, t_a) = a(T_a) \ln t_a + b(T_a). \tag{12}$$

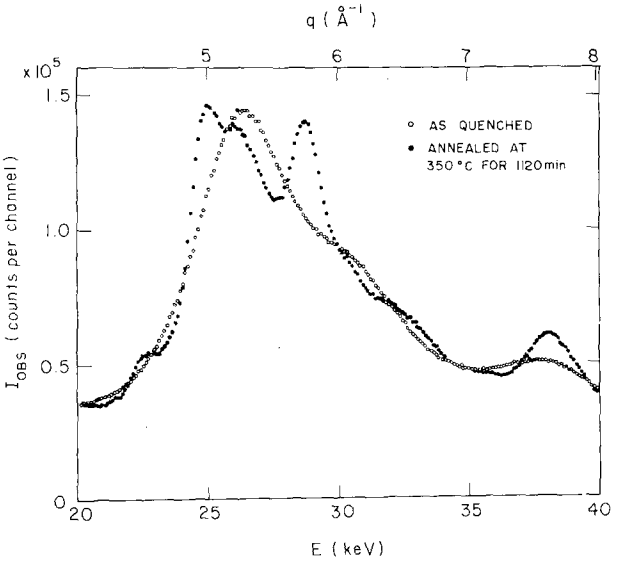

Figure 11 Change in the diffraction spectrum when the sample is partially crystalline.

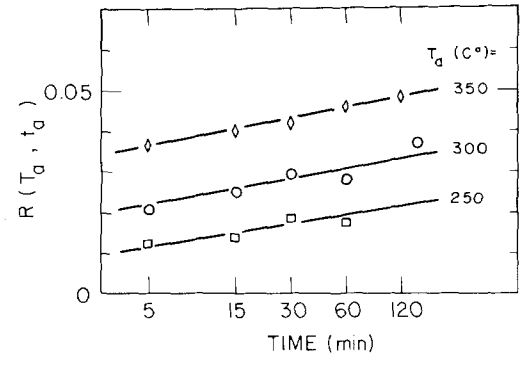

Figure 12 Kinetics of the relaxation parameter defined by Equation 11. Solid lines represents the fitting by Equation 15.

This logarithmic time dependence distinguishes it from the exponential time dependence of the single relaxation time first-order kinetics. The kinetics of the structural relaxation are usually interpreted in terms of widely distributed relaxation times. Instead, however, we propose a more collective and simpler description of the relaxation behaviour, by assuming that the apparent activation energy of the process is proportional to the total amount of the relaxation itself. The logarithmic time dependence, such as Equation 12, has been observed in certain cases of mechanical creep [37] and explained in terms of the exhaustion of the mobile lattice defects. Although the physical situations are different, the analyses made for the logarithmic creep [37–40] are quite useful for examining the present case.

If the rate of the change in a quantity x is described by a thermal activation process with an apparent activation energy which is proportional to x itself, i.e.,

$$dx/dt = c \exp(-\alpha x/kT) \qquad (13)$$

the kinetic equation is obtained by integration, as

$$x = \frac{kT}{\alpha} \ln(t + t_0) - \frac{kT}{\alpha} \ln \frac{kT}{c\alpha}. \qquad (14)$$

When this equation is applied to the structural relaxation process, the state described by $x = 0$ should correspond to the totally unrelaxed imaginary structure which could be obtained when the molten alloy was cooled down to $T = 0$ K at an infinitely high cooling rate. However, the cooling rate is finite and the measurements are usually made at room temperature, so that even in the as-quenched sample, a part of the structural relaxation should have occurred prior to the measurement. Therefore the equation for $R(T, t)$ should be,

$$R(T,t) = x - x_0 = \frac{kT}{\alpha} \ln(t + t_0) - \frac{kT}{\alpha} \ln \frac{kT}{c\alpha}$$

$$-x_0 = \frac{kT}{\alpha} \ln(t/t_0 + 1) \qquad (15)$$

where x_0 describes the structural relaxation of the as-quenched sample, and

$$t_0 = \frac{kT}{c\alpha} \exp\left(\frac{\alpha x_0}{kT}\right). \qquad (16)$$

If $t \gg t_0$, Equation 15 is reduced to Equation 12. This equation shows an excellent fit to the data (Fig. 11) when $\alpha/k = 1.72 \times 10^5$ K, $c = 10^{14.9}$ s^{-1}, and $x_0 = 0.122$. The values of t_0 are less than 0.03 min in this temperature range and are negligible. The apparent activation energy at $t = 0$, $\alpha x_0/k$, is equal to 2.1×10^4 K, or 1.8 eV. The value of x_0 is also a parameter to describe the quenching rate during the production process. Since the absolute value of x_0 depends upon the definition of the relaxation parameter, it is more convenient to express it in terms of the equivalent annealing necessary to bring the imaginary totally unrelaxed state to the actual as-received state. In the present case, the equivalent annealing condition is at 201° C for 1 min or at 167° C for 30 min. The value of c in Equation 13 should be of the order of the Debye frequency ($\sim 10^{13}$) times an appropriate constant to scale the magnitude of x (in this case, 1 to 10). Therefore the agreement is not poor. In fact the agreement is much better than in the case of the study of diffusion in which the pre-exponent was determined by conventional analysis without considering the structural relaxation, therefore it was found to be smaller by a factor of 10^6 than the appropriate value [41]. Equation 15 indicates that the structural relaxation is negligible at $T < 170$° C even after one hour of annealing, while diffusion appears to be appreciable at temperatures lower than 170° C [4, 17]. This is in accordance with our observation that the structural relaxation is a collective atomic process; diffusion is basically a single atomic process and does not necessarily result in the structural relaxation in a direct manner. On the other hand, the structural relaxation should control the decrease in the diffusivity. This point is evidenced by the fact that the range of annealing temperature in which the stress relaxation rate is appreciably reduced (Fig. 6 of [17]) agrees with the temperature range in which most of the structural relaxation takes place.

Thus, once we assume Equation 13, all the observed behaviour of the structural relaxation appears to be explained without any obvious discrepancy. Although there is no good *a priori* basis for it, the reason why Equation 13 can be valid is probably that the displacements of each atom with respect to the other atoms due to the structural relaxation is usually small, and therefore the change in the inter-atomic potential energy is linear with respect to the displacement, as is the activation energy.

6. Structural defects in amorphous alloys

The results presented in the last two sections describe features of atomic processes involved in the structural relaxation. The picture which seems to emerge from these results, however, is not in good harmony with the concept of free volume which was first introduced to explain the transport phenomena in liquid. For instance, a considerable amount of short-range ordering beyond the second nearest neighbour is taking place during the relaxation, while the change in the volume is minute. This indicates that the volume is no longer the most effective parameter to describe the structure of the metallic alloys below T_g. In fact, the microscopic definition of free volume by Turnbull and Cohen [6] strictly applies only above T_g where redistribution of free volume can be made without a change in the total internal energy. Below T_g, the excess free volume trapped in the glassy solid due to rapid quenching would partially or totally collapse, leaving internal strains around it. The centre of such internal strains is more like the structural defect in a crystalline solid than the free volume in a liquid which is in dynamic equilibrium and is not accompanied by static strains around it. Therefore we might call these centres structural defects, implying the deviation from the ideal fully-relaxed structure. The parameter defined by Equation 11, in our opinion, is a suitable parameter to describe the total density of the defects thus defined. Diffusivity or viscosity could be another effective parameter; the relation between them and $R(T, t)$ defined by Equation 11 has not yet been established. Strictly speaking, a fully relaxed structure is in most cases unattainable because the crystallization sets in before the structure becomes fully relaxed. However, the kinetics are logarithmic with time, and become progressively slower as they proceed. In the case of $Fe_{40}Ni_{40}P_{14}B_6$ alloy, therefore, the structure just before the start of the crystallization could be regarded as almost fully relaxed.

The structural defects thus defined help in an understanding of the structural relaxation and its kinetics in a most natural way. The structural relaxation is a process in which the quenched-in structural defects transform and redistribute

themselves into lower energy configurations. More specifically, they probably tend to split into smaller and more stable defects. This redistribution process is, unlike that of the free volume in liquid, irreversible and exothermic. A portion of these defects may find their way to a surface, resulting in a decrease in the specific volume, but most of them would continue to transform into smaller defects, and finally, will become a part of the stable amorphous structure.

7. Summary

Amorphous metallic alloys obtained by rapid cooling from the melt are known to undergo structural relaxation upon annealing at temperatures below the crystallization temperature. Observations of this structural relaxation have so far been mostly indirect, so that the phenomenon has not been understood at the atomic level. For the purpose of directly studying the changes in the atomic structure upon annealing, we have adopted the EDXD technique which offers high relative accuracy in the structural study of amorphous materials.

First, it was demonstrated that using the EDXD technique, one could determine the structure of amorphous alloy self-consistently. The RDF of $Fe_{40}Ni_{40}P_{14}B_6$ alloy thus obtained is in good agreement with the DRPHS model. Then, by way of the *in situ* annealing, the topological structural relaxation was studied in detail. It was found that the structural relaxation is a highly collective atomic process in which the relative configurations of groups of atoms (presumably structural units such as tetrahedra) are changed to stabilize themselves. The kinetics of the process (logarithmic in time) indicate that they can be best described in terms of the redistribution or transformation (splittings) of structural defects. Although the present study was made on one specific alloy composition, the conclusions are probably valid for other compositions too, at least for those amorphous alloys composed of the transition metals and metalloids, since the behaviour of the structural relaxation [16], and other kinetics [4, 5, 17, 23, 42, 43] does not depend upon details of the composition of the alloys.

Appendix

Determination of $\pi(E)$ and $\hat{I}_p(E)$

The determination of the polarizability $\pi(E)$ and the primary beam intensity $\hat{I}_p(E)$ becomes slightly more complicated when the Compton scattering is a significant portion of the total scattering by the sample. Rearranging Equation 1

$$\hat{I}_p(E) = I_s(E)/\left[P(E,\theta)(\langle f\cdot f^*\rangle + i(q)\langle f\rangle\langle f^*\rangle) + P(E',\theta)\langle f_c(q')\rangle \frac{2\hat{I}_p(E')/\hat{I}_p(E)}{1+\mu(E)/\mu(E')}\right]. \quad \text{(A1)}$$

Thus, in order to determine $\hat{I}_p(E)$ from the data, one has to know not only $\pi(E)$ but also $\hat{I}_p(E')/\hat{I}_p(E)$. Combining Equation 1 and Equation 5, one obtains

$$\pi(E') = \frac{R-1}{R+1}(1+X)/m - \pi(E)X \quad \text{(A2)}$$

where

$$m = \frac{1-\cos^2 2\theta}{1+\cos^2 2\theta} \quad \text{(A3)}$$

$$X = \frac{\langle f\cdot f^*\rangle + i(q)\langle f\rangle\langle f^*\rangle}{\langle f_c(q')\rangle \dfrac{2\hat{I}_p(E')/\hat{I}_p(E)}{1+\mu(E)/\mu(E')}} \quad \text{(A4)}$$

$$R = \frac{I_s^{\perp}}{I^{\parallel}} \quad \text{(A5)}$$

and $I_s^{\perp}$ is the intensity of the scattered X-ray with the scattering vector perpendicular to the plane of polarization (the plane which includes the direction of the electron beam in the X-ray tube), and $I_s^{\parallel}$ is the intensity with the scattering vector parallel to the plane of the polarization. Then $\pi(E')$ also can be determined only when we know other quantities such as $\hat{I}_p(E')/\hat{I}_p(E)$.

We used data from four runs to determine self-consistently $\pi(E)$ and $\hat{I}_p(E)$ using these equations. These were runs at $\theta_1 = 30.92°$, $\theta_2 = 34.94°$, and runs at $\theta_3 = 42.40°$, but with parallel and perpendicular scattering conditions. The former two angles were chosen so that the oscillations in $i(q)$ as functions of E are opposite in phase. The data at θ_3 were used to calculate R. First, assuming $i(q) = 0$ and $\hat{I}_p(E')/\hat{I}_p(E) = 1$, $\pi(E')$ was calculated using Equation A2 repeatedly until it converged. Then using $\pi(E)$ thus obtained, $\hat{I}_p(E')/\hat{I}_p(E) = 1$ for θ_1 and θ_2 using Equation A1. $\hat{I}_p(E)$ were averaged over the two results and reiterated into Equation A1 until it converged. $\pi(E')$ was then recalculated, using values of $\hat{I}_p(E)$. After two such paths, both $\pi(E)$ and $\hat{I}_p(E)$ reached self-consistency within the error of 10^{-3}. Polynomials with seven parameters

were fitted by the least square method to $\pi(E)$ and $\hat{I}_p(E)$, to remove noise and remaining structures. The results are given in Figs. 3 and 4. Since the polarization of the primary beam was found to be significant enough to influence the accuracy of the data, it may be advisable in future measurements to use the X-ray tube tilted at an angle of 45° away from the diffraction plane, that is the plane which includes the primary and diffracted beams. The polarization factor would then be independent of the diffraction angle, simplifying the analysis significantly.

Acknowledgements

The author is thankful to T. Ichikawa for technical assistance in setting up the EDXD system and for helpful suggestions, to J. T. Prater for help in designing the system, and to H. Katz for maintenance of the X-ray generator. He also gratefully acknowledges C. D. Graham, Jr, and Y. Waseda for discussions and comments on the manuscript, and to H. S. Chen for useful discussions.

References

1. P. DUWEZ, *Ann. Rev. Mater. Sci.* 6 (1976) 83
2. J. J. GILMAN, *Phys. Today* 28 (1975) 46.
3. T. EGAMI, P. J. FLANDERS and C. D. GRAHAM Jr., *AIP Conf. Proc.* 24 (1975) 697.
4. F. E. LUBORSKY, J. J. BECKER and R. O. McCARY, *IEEE Trans. Mag.* **MAG-11** (1975) 1644.
5. C. D. GRAHAM Jr., T. EGAMI, R. S. WILLIAMS and Y. TAKEI, *AIP Conf. Proc.* 29 (1976) 218.
6. M. H. COHEN and D. TURNBULL, *J. Chem. Phys.* **31** (1959) 1164.
7. *Idem, ibid.* **34** (1961) 120.
8. F. SPAEPEN and D. TURNBULL, in "Rapidly Quenched Metals", edited by N. J. Grant and B. C. Giessen (MIT Press, Cambridge, 1976) p. 205.
9. M. GOLDSTEIN, in "Modern Aspects of the Vitreous State", edited by J. D. MACKENZIE, Vol. 3 (Butterworth, Washington, 1964) p. 90.
10. S. E. PETRIE, in "Polymeric Materials", (American Society for Metals, Metals Park, 1975) p. 55.
11. A. J. KOVACS, R. A. STRATTON and J. D. FERRY, *J. Phys. Chem.* 67 (1963) 152.
12. H. EYRING, *J. Chem. Phys.* 4 (1936) 283.
13. H. S. CHEN, H. J. LEAMY and M. BARMATZ, *J. Non-Cryst. Solids* 5 (1970) 444.
14. T. SOSHIRODA, M. KOIWA and T. MASUMOTO, *ibid.* 22 (1976) 173.
15. B. S. BERRY, in "Metallic Glasses", edited by H. J. Leamy and J. J. Gilman (American Society for Metals, Metals Park, 1978) p. 161.
16. H. S. CHEN and E. COLEMAN, *Appl. Phys. Lett.* **28** (1976) 245.
17. R. S. WILLIAMS and T. EGAMI, *IEEE Trans Mag.* **MAG-12** (1976) 927.
18. R. MADDIN and T. MASUMOTO, *Mater. Sci. Eng.* 9 (1972) 153.
19. Y. WASEDA and T. MASUMOTO, *Z. Physik* **B22** (1975) 121.
20. J. F. CRACZYK, *J. Appl. Phys.* **49** (1978) 1738.
21. Details of the production process of the Metglas alloys are not published, but are believed to be similar to the one described by H. H. LIEBERMANN and C. D. GRAHAM Jr., *IEEE Trans. Mag.* **MAG-12** (1976) 921.
22. T. EGAMI, *Mater. Res. Bull.* **13** (1978) 557.
23. H. H. LIEBERMANN, C. D. GRAHAM Jr. and P. J. FLANDERS, *IEEE Trans. Mag.* **MAG-13** (1977) 1541.
24. B. C. GIESSEN and G. E. GORDON, *Science* **159** (1968) 973
25. J. M. PROBER and J. M. SCHULTZ, *J. Appl. Cryst.* 8 (1975) 405.
26. H. P. KLUG and L. E. ALEXANDER, "X-ray Diffraction Procedures for Polycrystalline and Amorphous Materials", 2nd edition (John Wiley, New York 1974).
27. "International Tables for X-ray Crystallography", Vol. 3 and 4 (The Kynoch Press, Birmingham, 1962, 1974).
28. D. T. CROMER and D. LIEBERMAN, Los Alamos Scientific Laboratory Report, LA-4403 (1970).
29. L. G. PARRATT and C. F. HEMPSTEAD, *Phys. Rev.* 94 (1954) 1593.
30. D. T. CROMER and J. B. MANN, *J. Chem. Phys.* 47 (1967) 1892.
31. D. T. CROMER *ibid.* 50 (1969) 4857.
32. B. E. WARREN, "X-Ray Diffraction" (Addison-Wesley, Reading, Mass, 1969).
33. T. ICHIKAWA, *Phys. Stat. Sol.* **a29** (1975) 293.
34. G. S. CARGILL, in "Solid State Physics", edited by Ehrenreich, F. Seitz and D. Turnbull, Vol. 30 (Academic Press, New York, 1975) p. 227.
35. Y. WASEDA, H. OKAZAKI, M. NAKA and T. MASUMOTO, *Sci. Rep. RITU* **A26** (1976) 12.
36. T. EGAMI and T. ICHIKAWA, *Mater. Sci. Eng.* **32** (1978) 293.
37. J. M. ROBERTS and N. BROWN, *Acta Met.* 11 (1963) 7
38. W. KAUZMANN, *Trans. AIME* **143** (1941) 57.
39. N. F. MOTT, *Phil. Mag.* 44 (1953) 742.
40. A. SEEGER, *Z. Naturforsch* **9a** (1954) 758.
41. D. GUPTA, K. N. TU, and K. W. ASAI, *Phys. Rev. Lett.*, **35** (1975) 796.
42. L. A. DAVIS, R. RAY, C. P. CHOU and R. C. O'HANDLEY *Script. Met.* **10** (1976) 541.
43. T. EGAMI, *J. Amer. Ceramic Soc.* **60** (1977) 128.

Received 13 February and accepted 10 March 1978.